

# Techniques for Modeling Muscle-Induced Forces in Finite Element Models of Skeletal Structures

IAN R. GROSSE,<sup>1\*</sup> ELIZABETH R. DUMONT,<sup>2</sup> CHRIS COLETTA,<sup>1</sup>  
AND ALEX TOLLESON<sup>1</sup>

<sup>1</sup>Department of Mechanical and Industrial Engineering, University of Massachusetts  
Amherst, Amherst, Massachusetts

<sup>2</sup>Department of Biology, University of Massachusetts Amherst, Amherst, Massachusetts

---

---

## ABSTRACT

This work introduces two mechanics-based approaches to modeling muscle forces exerted on curvilinear bone structures and compares the results with two traditional ad hoc methods of muscle loading. These new models use a combination of tensile, tangential, and normal traction loads to account for muscle fibers wrapped around curved bone surfaces. A computer program was written to interface with a commercial finite element analysis tool to automatically apply traction loads to surface faces of elements in muscle attachment regions according to the various muscle modeling methods. We modeled a highly complex skeletal structure, the skull of a Jamaican fruit bat (*Artibeus jamaicensis*), to compare the four muscle-loading methods. While reasonable qualitative agreement was found in the states of stress of the skull between the four muscle load modeling methods, there were substantial quantitative differences predicted in the stress states in some high stressed regions of the skull. Furthermore, our mechanics-based models required significantly less total applied muscle force to generate a bite-point reaction force identical to those produced by the ad hoc muscle loading models. Although the methods are not validated by in vivo data, we submit that muscle-load modeling methods that account for the underlying physics of muscle wrapping on curved bone surfaces are likely to provide more realistic results than ad hoc approaches that do not. We also note that, due to the geometric complexity of many bone structures—such as the skull analyzed here—load transmission paths are difficult to conceptualize a priori. Consequently, it is difficult to predict spatially where the results of finite element analyses are likely to be compromised by using ad hoc muscle modeling methods. For these reasons, it is recommended that a mechanics-based method be adopted for determination of the proper traction loads to be applied to skeletal structures due to muscular activity. Anat Rec, 290:1069–1088, 2007. © 2007 Wiley-Liss, Inc.

**Key words:** finite element analysis; muscle force; skull; muscle loading algorithm, biting

---

---

Finite element analysis (FEA) is a numerical tool that engineers use to investigate the behavior of physical systems such as engineered products and manufacturing processes. As a predictive analysis tool, FEA has developed to the point where high technology companies now rely on it heavily to reduce or eliminate expensive and time-consuming prototype fabrication and testing (Ulrich and Eppinger, 2000). Very recently, comparative biolo-

Grant sponsor: NSF; Grant number: IOB 0447616.

\*Correspondence to: Ian R. Grosse, Department of Mechanical and Industrial Engineering, University of Massachusetts Amherst, 160 Governor's Drive, Amherst, MA 01003. Fax: 413-545-1027. (no). E-mail: grosse@ecs.umass.edu

Received 27 February 2007; Accepted 4 June 2007

DOI 10.1002/ar.20568

Published online in Wiley InterScience (www.interscience.wiley.com).

gists have recognized the utility of FEA for predicting the behavior of complex systems and are beginning to use it to investigate the functional adaptations of living organisms (Korioth et al., 1992; Spears et al., 1993; Wootton et al., 2003; Witzel et al., 2004; Dumont et al., 2005; Metzger et al., 2005; Richmond et al., 2005; Strait et al., 2005) and to reconstruct the behaviors of extinct organisms (Richmond and Qin, 1996; Fastnacht et al., 2002; Preuschoft and Witzel, 2004; Rayfield, 2004, 2005).

Despite advances driven by the biomedical industry (Teran et al., 2005), building three-dimensional finite element models of complex biological structures remains complicated and time consuming. In an effort to streamline the process, finite element analyses that include muscle-induced forces have taken one of two different modeling approaches. The first is to directly model muscles using finite elements. Muscle is a kinematically, geometrically, and materially complex tissue. The primary goal of these studies is to describe how muscles change shape and produce work (Blemker and Delp, 2005; Blemker et al., 2005; Lemos et al., 2005). Modeling studies that focus on muscles understandably place less emphasis on developing complicated models of bone. The second approach to including muscle force in FEAs has been to model muscles indirectly by applying forces at points in muscle attachment regions or tractions to areas of muscle attachment on FE models of bone (Rayfield, 2004; Dumont et al., 2005; Metzger et al., 2005; Ross et al., 2005; Strait et al., 2005). This method is favored by comparative and evolutionary biologists whose interests lie in understanding the functional implications of bone shape.

The goal of this study is to determine whether different methods of applying muscle forces to a complex bone model produce substantially similar results. If so, then researchers can use the simplest (and least time-intensive) technique with some degree of confidence. On the other hand, very different results would indicate that the decision to use a particular method of applying muscle force should be considered carefully. In this study, we compare results derived from four methods of applying muscle forces to a detailed finite element model of a skull. The first two methods are already used widely and are based on ad hoc assignment of point loads or traction loads for each muscle attachment area. We developed two new methods of applying muscle forces that are based on the underlying mechanics of how muscle fibers interact with the underlying bone. Specifically, the methods account for the fact that muscles wrap around the skull surface and impose tangential and normal loads on it.

## MATERIALS AND METHODS

### Finite Element Model

We built a finite element model of the skull of a Jamaican fruit bat (*Artibeus jamaicensis*) by a multistep process that required several different software applications. To begin, a series of 874 two-dimensional grayscale bitmap images of the skull were collected from an alcohol-preserved specimen using high-resolution computed tomography (micro-CT) scanner (Skyscan model 1172). Adjacent images were separated by 0.019 mm. The stack of images was used to reconstruct a three-dimensional digital representation of the skull surface in the software package Amira 3.1.1 (Mercury Computer

Systems, Inc., Chelmsford, MA). The three-dimensional Amira file was then exported in stereo-lithography (stl) format and opened in the next software package we used, Geomagic Studio9 (Geomagic, Inc, Research Triangle Park, NC). Studio8 was used to “clean” the surface representation. Cleaning the surface representation involved resolving digital reconstruction errors and simplifying or eliminating some of the skull’s anatomical, nonstructural, features. Once the surface model was sufficiently clean to form a water-tight volume, we again exported it as a stereo-lithography file and imported it into the FEA software, Strand7 (G+D Computing Pty Ltd, Sydney, Australia). Strand7 was then used to automatically generate a solid mesh of the skull composed of four-noded linear tetrahedral elements. The final volumetric model contained 1,133,096 tetrahedral elements, 247,854 nodes and 743,553 active degrees of freedom.

We assigned material properties to the model using a rationale outlined in a previous study (Dumont et al., 2005). Briefly, we assigned average values of Young’s modulus ( $E = 2 \times 1010$  Pa) and Poisson’s ratio ( $\nu = 0.3$ ) for mammalian bone (Erickson et al., 2002) to the skull model. We further assumed that the bone of the skull was homogeneous and isotropic. Constraints were applied to the skull following methods introduced by Strait et al. (2002) and subsequently used in several analysis of mammalian masticatory mechanics (Dumont et al., 2005; Ross et al., 2005; Strait et al., 2005). Briefly, reaction forces at the temporomandibular joints (TMJs) were modeled by constraining a single node in the center of each TMJ against displacement. This created an axis around which the skull rotated when muscle forces were applied. This constraint is consistent with rigid body mechanics perspective of the skull having an instantaneous axis of rotation for a given gape. To prevent this rigid body motion and induce elastic deformation due to biting forces, a node at the tip of the upper right first molar was constrained against displacement (i.e., displacements in the  $x$ -,  $y$ -, and  $z$ -planes were set equal to 0). Note that these single-node constraints at the TMJ joints and bite tooth will produce artificially high strain and stress values in the near vicinity of these locations. Yet, due to Saint Venant’s principle (Malvern, 1969) this effect is highly localized and will not influence the global stress and strain state throughout the skull.

Based on studies of muscle activity in another large bat and in primates (De Gueldre and De Vree, 1988; Hylander et al., 2004), we assumed simultaneous, maximum, and bilateral activity of the temporalis, masseter, and medial pterygoid muscles and applied muscle forces to the skull in proportion to their relative physiological cross-sectional areas (PCSA; temporalis = 69%, masseter = 9%, and medial pterygoid = 22%; unpublished data from A. Herrel). Although this loading regimen is unlikely to occur during routine chewing, it may approximate loading conditions during hard-object feeding. Moreover, variation in the relative contributions of different muscles to peak bite force has been shown to have only a nominal effect on patterns of strain predicted in FE analyses (Ross et al., 2005).

### Modeling Muscle Loads

There are two distinct ways to model muscle loading on the skull: a direct “physical” approach and an indi-

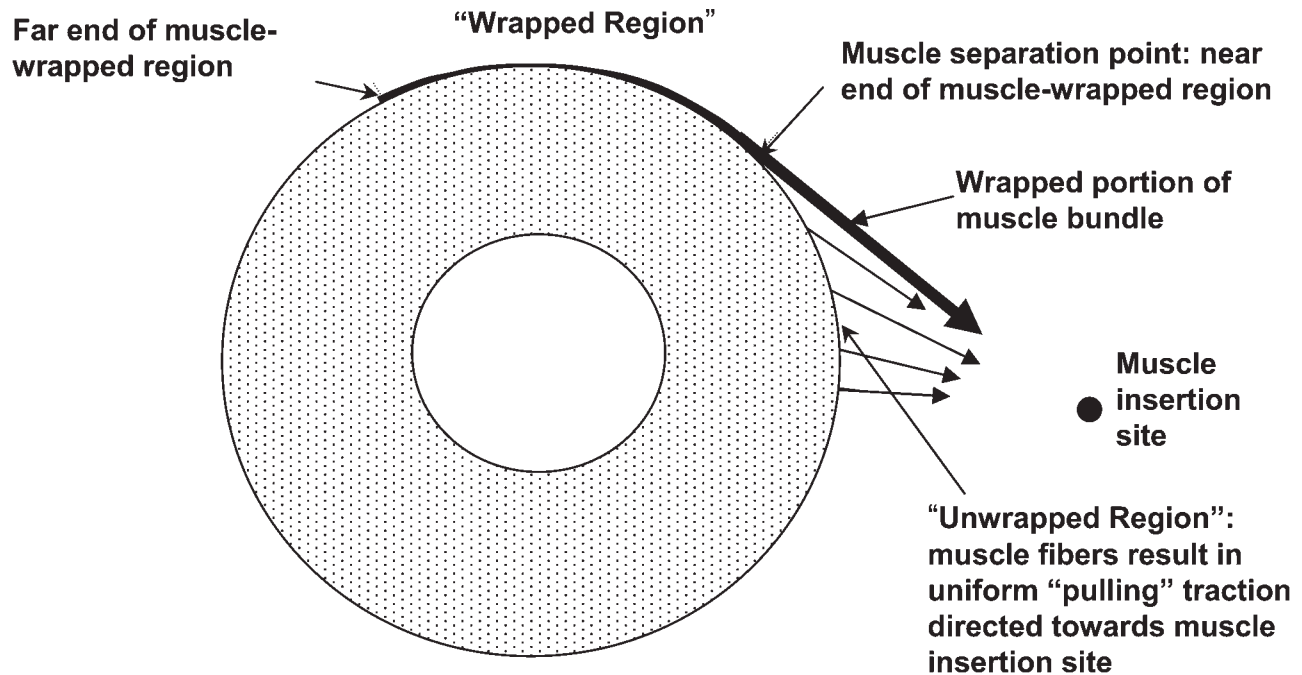


Fig. 1. Simplified illustration of muscle wrapping around a bone.

rect mechanics approach. In the direct approach, the soft muscle tissue is included in the analysis model as a separate meshed geometrical entity with the proper anisotropic material properties specified. Unfortunately, this approach greatly complicates the digital reconstruction process, as now the geometries defining both bone material and the soft muscle tissue need to be extracted from the CT scans. Furthermore, the fibers within each muscle are complexly interwoven and exhibit complex hyperelastic, anisotropic, and incompressible material behavior (Johansson et al., 2000; Teran et al., 2003; Zhou and Lu, 2005). Including these details in a highly detailed geometrical skull model would add a level of complexity that is beyond the scope of this study. Moreover, because our focus is on the response of the skull, such detailed modeling of the muscles themselves may not be necessary.

We advocate a much simpler indirect mechanics approach in which the muscles are not included in the model. Instead, we account for the effect of the muscles' contractions by applying forces or tractions (forces per unit area) to the skull in areas of muscle attachment and in the direction of the muscle fibers toward points of attachment on the lower jaw. We investigated the effects of four different indirect muscle loading methods on the stress and strain behavior of the skull due to bite forces. Each muscle loading method corresponded to a different level of abstraction. In each of our models, we loaded the skull with all three paired muscle groups and treated the problems as linear elastostatic analyses, assuming that the muscle groups fire bilaterally and simultaneously; dynamic effects were neglected. The four different models for indirect muscle loads are (1) an ad hoc point-load model, (2) an ad hoc uniform traction load model,

(3) a tangential-traction load model, and (4) a tangential-plus-normal-traction load model.

#### Ad hoc Point-Load Model

In this model, we applied point loads to finite element nodes at ad hoc locations in the muscle skull attachment areas. Three point loads of equal magnitude were applied at ad hoc locations in each muscle bundle attachment area on the skull and directed toward the appropriate attachment point on the lower jaw.

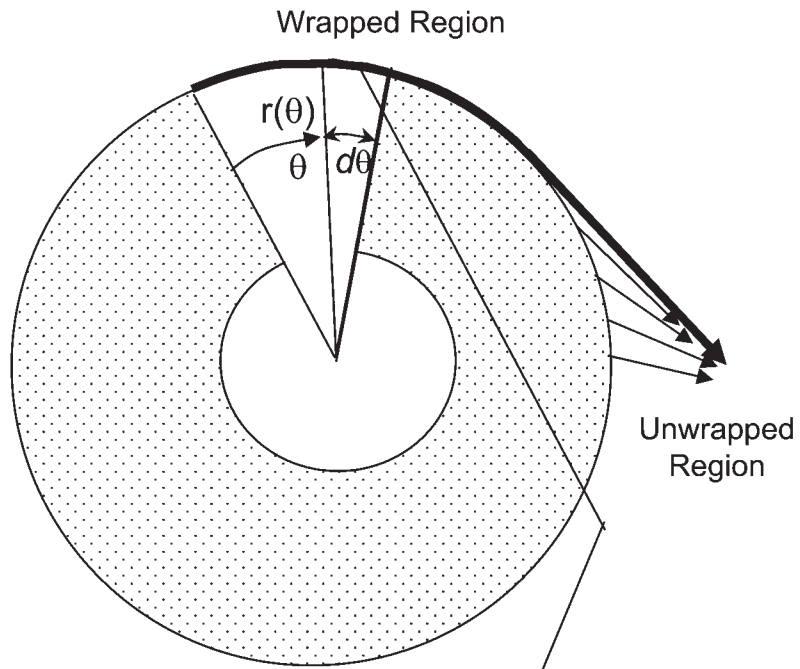
#### Ad hoc Uniform Traction Model

In this model, we applied uniform traction to the surfaces of finite elements that represent the muscle attachment areas. The direction of the traction load is not normal to the surface of the element. Rather, the direction of traction varied from element to element such that the traction load is always directed toward the force focal node of each muscle attachment group.

#### Tangential-Traction Model

This model sought to account for the mechanics of muscle fibers wrapping around portions of the skull (Figs. 1, 2). We assumed that individual muscle fibers are uniformly distributed and uniformly 'anchored' to the skull in regions of muscle attachment. This meant that the traction applied to each element face was identical within each muscle attachment region. If the unit outward normal for a surface finite element in the muscle attachment region had a "clear line of sight" to the lower-jaw attachment point, then we applied traction to that element's surface face in the direction to the force

A)



B)

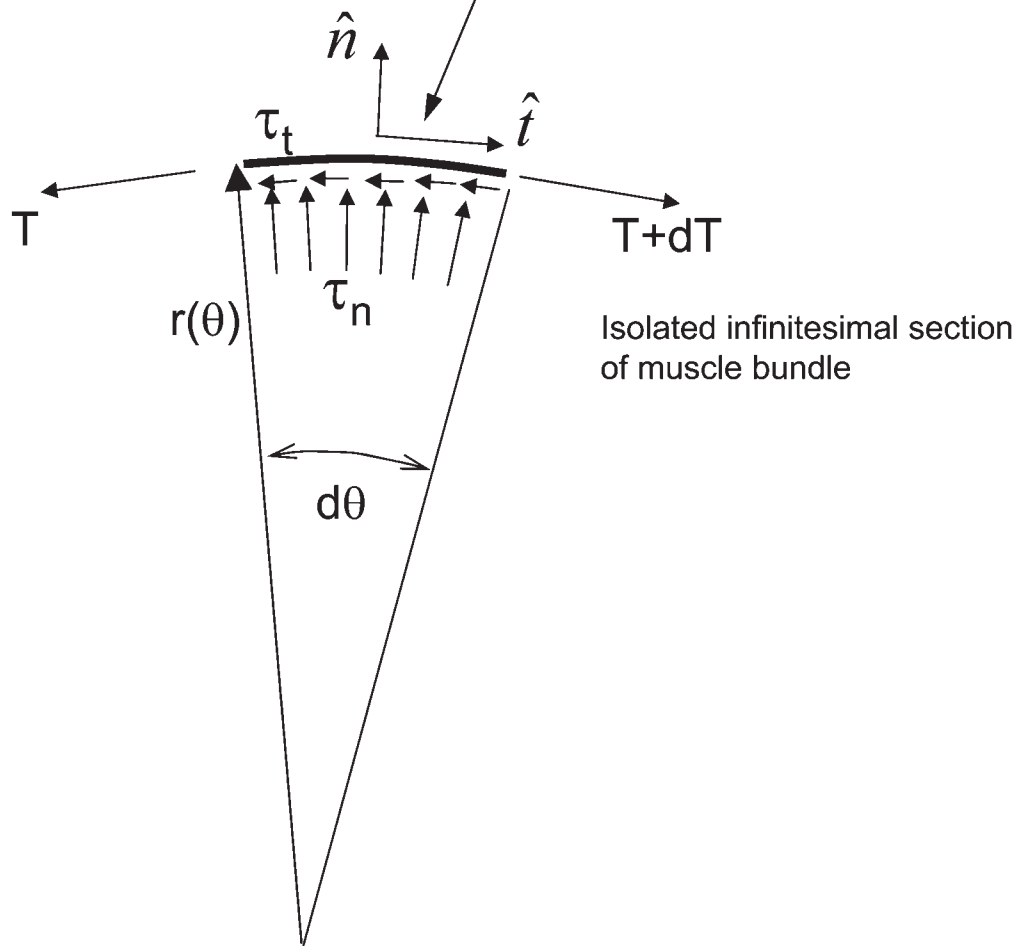


Fig. 2. **A:** Simplified model of a bone segment with a muscle wrapped around it. **B:** A free body diagram of an isolated infinitesimal section of muscle spanning an angle  $d\theta$  showing normal and tangential tractions exerted upon it by the underlying skull.

focal node that defines the attachment point on the lower jaw. However, when the face of the finite element did not have a direct line of sight to the point of muscle attachment on the lower jaw, then muscle fibers were assumed to wrap across the element face. The anchoring of muscle fibers to the skull in this “wrapped region” results in a tangentially directed traction in the fiber bundle direction. The total tangential force applied to an element is simply the tangential traction exerted by the anchored fibers times the area of that element’s face. The direction of the tangential traction varies from element to element and was computed by vector mathematics. The value of uniform traction applied to each muscle attachment region was based on the total muscle force for the muscle group divided by the surface area of the attachment region.

### Tangential-Plus-Normal-Traction Model

The tangential-traction model differs significantly from the point and distributed load models. However, it still neglects the normal traction (i.e., pressure) that muscle fibers impose on the skull as they wrap around it. Many fibers that are anchored elsewhere may pass over any given segment of the skull. In addition to exerting a tangential traction, fibers that wrap across the surface must also exert a traction normal to skull or, in our finite element model, normal to the surface face of a wrapped element. We used a physics-based approach to derive a formula for this normal traction. Let  $\vec{r}$  be a position vector that locates the centroid of the surface face of a wrapped element. A nonuniform normal traction,  $\tau_n(\vec{r})$ , was applied on surface faces of all wrapped elements in each muscle attachment region given by the formula:

$$\tau_n(\vec{r}) = \left( \frac{s(\vec{r})}{R(\vec{r})} \right) \tau_t \quad (1)$$

where  $\tau_t$  is the uniform tangential traction applied to the muscle attachment region,  $s(\vec{r})$  is the path length from the far end of the muscle attachment region to the current element surface, and  $R(\vec{r})$  is the instantaneous radius of curvature of the muscle fiber in the direction of the muscle fiber. This formula is derived in the appendix based on fundamental principles of equilibrium.

We assumed that the radius of the curvature of the wrapped muscle is identical to the skull’s radius of curvature, except in the vicinity of the near end of the muscle attachment region where the muscle begins to separate from the skull. Various methods can be used to estimate the principal radii of curvature of a polygonal surface (i.e., the surface faces of tetrahedral elements in the muscle attachment regions) (Razdan and Bae, 2005). We used data from adjacent elements and vector mathematics to generate a reasonable approximation of the skull radius of curvature in the direction of the tangential traction for each surface face of the finite elements in the region of muscle attachment.

A much more tedious calculation to perform is determining the path length  $s(\vec{r})$ . Recall that  $s(\vec{r})$  is the path length in the direction of the muscle fiber bundle along the surface of the skull, beginning from the far end of the muscle attachment region to the centroid of the cur-

rent surface face location in the muscle attachment region, denoted by  $\vec{r}$ . The surface of the skull was approximated by a piecewise triangulation which comprised the surface faces of the tetrahedral mesh. To compute the surface path length for each muscle-wrapped tetrahedral element, we defined an infinite plane given by the unit normal vector to the surface face of the current tetrahedral element and the focal point of the muscle group. The intersection of this plane with the triangulation of the surface skull contains the path from the far end of the muscle attachment area to the current element. An algorithm with the necessary logic and vector mathematics was developed to compute this path length for the surface face of each wrapped element of each muscle group.

Because the surface faces of thousands of finite elements model the various muscle attachment regions, an automated procedure is needed to apply tractions that vary in direction and magnitude element by element. For this purpose a Microsoft Visual Basic program, called BoneLoad (the BoneLoad executable code may be downloaded for free at [www.biomech.org](http://www.biomech.org)) was created to facilitate the implementation of these muscle loading models with a commercial FEA tool. BoneLoad allows the user to automatically assign ad hoc uniform traction loads forces, tangential-traction loads, or a combination of tangential-plus-normal-traction loads to the free surfaces of tetrahedrals located in the muscle attachment regions of the skull. The program exploits the Application Programming Interface (API) of the Strand7 finite element code to read the necessary mesh information of the model, performs the necessary calculations to determine traction values and directions for surface faces of every element in every muscle attachment region, and writes these tractions directly to the finite element model’s binary database file. Figure 3 presents an example of the tangential and normal loads applied by the BoneLoad program.

To make comparisons among the four muscle loading models, we adjusted the overall magnitude of muscle forces applied to each model until a reaction force of 22.5N was generated perpendicular to the palate at the constrained node on the upper right molar (Dumont et al., 2005). This requires two separate FEAs. Each muscle group is assumed to apply a muscle force proportional to its PCSA value. Thus, in the first analysis we let

$$F_i = \left( \frac{PCSA_i}{\sum_{i=1}^m PCSA_i} \right) F_{initial} \quad (2)$$

where  $F_i$  is the amount of muscle force applied to muscle group  $i$ ,  $PCSA_i$  is the PCSA value for muscle group  $i$ ,  $m$  total number of muscle groups, and  $F_{initial}$  is an arbitrary force value. The solution of this analysis gives a reaction force value  $R$  in the measured bite force direction at the constrained tooth node corresponding to the bite point that is directly proportional to  $F_{initial}$ . In the second analysis, all muscle group forces are then scaled by the ratio of  $R_{actual}/R$ , where  $R_{actual}$  is the average bite force measured in the field using a portable force transducer of *Artibeus jamaicensis* during voluntary

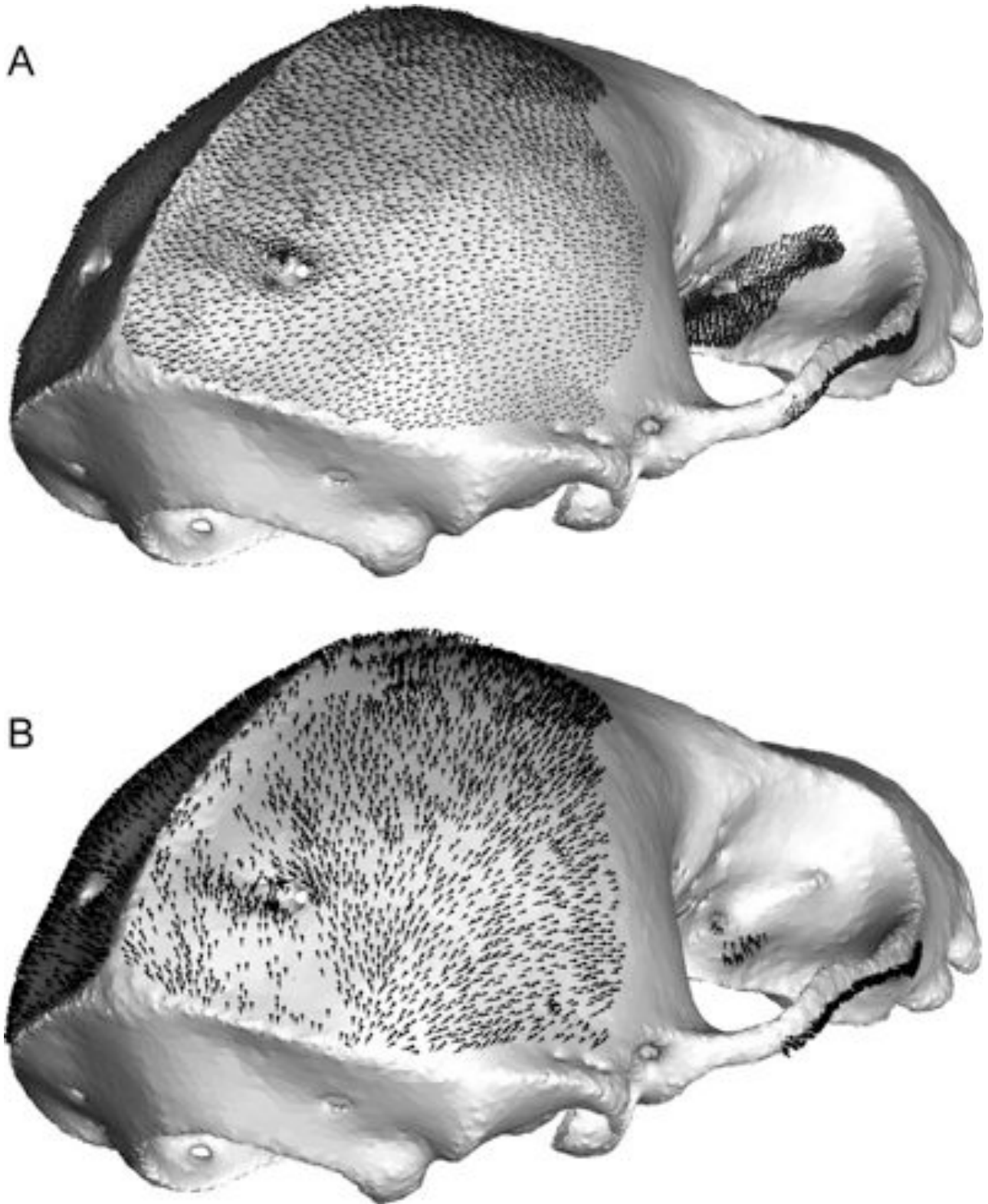


Fig. 3. **A,B:** Tangential (A) and normal (B) loads distributed over the attachment region of the right temporalis muscle using the BoneLoad program. Arrowheads indicate distribution and directions of tractions; magnitudes are not shown.

**TABLE 1. Comparative static analysis metrics for the four muscle loading models. All models were loaded to generate a 22.5 N reaction force in the direction of bite force direction at the constrained node on the right upper first molar**

Item	Units	Muscle loading models			
		<i>ad hoc</i> point load	<i>ad hoc</i> traction	Tangential traction	Tangential normal traction
$F_{temporalis}^1$ (% of $F_{total}$ )	N (%)	24.5 (68.5)	25.2 (68.6)	19.8 (68.4)	21.9 (68.6)
$F_{masseter}^2$ (% of $F_{total}$ )	N (%)	2.86 (8.00)	2.96 (8.10)	2.36 (8.20)	2.61 (8.20)
$F_{pterygoid}^3$ (% of $F_{total}$ )	N (%)	8.39 (23.5)	8.56 (23.3)	6.79 (23.5)	7.43 (23.3)
$F_{total}^4$	N	35.8	36.72	29.0	31.9
$\eta_{load}^5$	%	76.6	73.4	100	90
$\theta_{temporalis}^6$	deg	3.55	1.78	23.19	2.45
$\theta_{masseter}^7$	deg	3.69	3.15	9.06	2.95
$\theta_{pterygoid}^8$	deg	0.93	0.98	1.11	1.84
$M_{LTMJ}^9$	N mm	332.2	323.9	247.9	299.8
$M_{RTMJ}^{10}$	N mm	339.8	333.3	257.3	292.9
$M_{TMJA}^{11}$	N mm	231.3	214.5	209.5	200.1
$\eta_{moment}^{12}$	%	68.9	65.3	83.0	67.5

<sup>1</sup> $F_{temporalis}$  is the average value of the magnitudes of the total left and right temporalis muscle forces.

<sup>2</sup> $F_{masseter}$  is the average value of the magnitudes of the total left and right masseter muscle forces.

<sup>3</sup> $F_{pterygoid}$  is the average value of the magnitudes of the total left and right pterygoid muscle forces.

<sup>4</sup> $F_{total} = F_{temporalis} + F_{masseter} + F_{pterygoid}$ .

<sup>5</sup> $\eta_{load}$  is the relative muscle load efficiency as defined in Equation (4).

<sup>6</sup> $\theta_{temporalis}$  is the angle between temporalis muscle force vector and vector from muscle area centroid to muscle.

<sup>7</sup> $\theta_{masseter}$  is the angle between masseter muscle force vector and vector from muscle area centroid to muscle focal.

<sup>8</sup> $\theta_{pterygoid}$  is the angle between pterygoid muscle force vector and vector from muscle area centroid to muscle focal.

<sup>9</sup> $M_{LTMJ}$  is the magnitude of the moment exerted by all the muscle forces about the left TMJ.

<sup>10</sup> $M_{RTMJ}$  is the magnitude of the moment exerted by all the muscle forces about the right TMJ.

<sup>11</sup> $M_{TMJA}$  is the magnitude of the moment due to all applied muscle forces about the TMJ axis.

<sup>12</sup> $\eta_{moment}$  is the moment efficiency of the applied muscle loads as defined by Equation (5).

unilateral molar biting (Aguirre et al., 2002; Dumont and Herrel, 2003):

$$F_i = \left( \frac{PCSA_i}{\sum_{i=1}^m PCSA_i} \right) \left( \frac{R_{actual}}{R} \right) F_{initial} \quad (3)$$

Because the reaction force  $R$  obtained in the first analysis is directly proportional to  $F_{initial}$ , the result of the second analysis is a reaction force value at the bite tooth node exactly equal to  $R_{actual}$ —the experimentally measured value—irrespective of the  $F_{initial}$  value. This strategy allowed us to compare the absolute magnitudes of the muscle forces required to generate a realistic bite force as well as the effect of those forces on the distribution and magnitude of stress in the finite element model. Each of the four muscle loading models was solved using the linear static solver provided in Strand7 (GD Computing Pty Ltd., Sydney, Australia).

## RESULTS

### Model Comparison Based on Static Analysis

Before comparing strain and stress analysis results based on the four different loading scenarios, it is important to note any differences between the loading scenarios from a system-level perspective. To this end, we developed several system-level metrics related to the forces applied to the model by the four muscle modeling methods (Table 1). These metrics include total muscle force applied to the skull for each muscle group, the

degree in which this force vector is aligned toward the muscle group force focal node, the moment about the left and right TMJ and the TMJ axis exerted by each muscle group, and two muscle loading efficiency metrics as defined below.

First, from each analysis we extracted data summarizing the magnitudes of total muscle forces that were applied to the models to generate 22.5 N of bite force at the constrained molar and in the same direction for which we had obtained bite force data through in vivo measurement. Values of these force magnitudes for each muscle group, averaged across the left and right, are shown in the first three rows of Table 1. The force magnitude for each muscle attachment region is the magnitude of the vector sum of all the applied forces to the attachment region. Note that, in all the models, the relative magnitude of forces across muscle groups closely matched the desired 69% temporalis, 9% masseter, and 22% pterygoid force ratios.

Data presented in Table 1 illustrate that the tangential traction model required the least amount of applied muscle loads, as measured by  $F_{total}$ , to achieve the same bite reaction force. The tangential-plus-normal-traction model required approximately 10% more applied muscle force, and the two *ad hoc* models required approximately 25–27% more applied muscle forces to generate the same unilateral molar bite reaction force. We defined

$$\eta_{load} \equiv 100 \left( 1 - \frac{F_{total} - \min(F_{total})}{\min(F_{total})} \right) \quad (4)$$

as the relative efficiency of the applied muscle forces for a given modeling method, where  $F_{total}$  is the total applied

muscle forces for a given muscle modeling method, and  $\min(F_{total})$  is the minimum total applied muscle force magnitudes among all the modeling methods.

Also shown in Table 1 are degrees of muscle force alignment, moments of the total force vector applied for each muscle group about the left and right TMJs, the moment of each total force vector applied for each muscle group about the TMJ axis, and the efficiency of the muscle forces about the TMJ axis. For all of these metrics, we assumed that the total force applied to the skull for each muscle group, which is either due a collection of point loads or due to a set of traction loads (i.e., surface loads per unit area), acts at the geometric centroid of the skull's muscle attachment region. The degree of alignment is defined as the angle between the total muscle force vector for each muscle attachment region and the vector from the geometric centroid of the region to the force focal node of that region. With the exception of the tangential-traction-only model, the total applied force vector to the region was well aligned toward the region's force focal node. In the tangential-traction-only model, tangential tractions applied to the regions of muscle attachment were misaligned up to 23.19 degrees for the temporalis muscle group.

The magnitudes of moments exerted by the applied loads about the left and right TMJs indicate that excellent bilateral load symmetry was achieved for all models (Table 1). Considering that the sizes, shapes, and locations of muscle attachment regions and the force focal node locations were all identified visually, the bilateral agreement of exerted moments about the TMJs is quite good.

Moment results also indicate that applied muscle loads for the point load and ad hoc traction models exerted very comparable moment magnitudes about the left and right TMJs, and that these moment magnitudes were larger than the moment magnitudes produced by the tangential-traction and the tangential-plus-normal-traction models. Recall that a moment is a vector with a magnitude and direction. The moment about the axis defined by the TMJs, found in the penultimate row of Table 1, is the component of this vector along the direction of the joint axis. This is the portion of the total moment due to all the applied muscle loads that produces pure rotation about the TMJ axis. We defined  $\eta_{moment}$  as the moment efficiency of the applied muscle loads and calculated it as the percentage of total applied moment due to the muscle forces that results in a pure rotational moment about the TMJ axis:

$$\eta_{moment} = 100 \left( \frac{M_{mja}}{\frac{1}{2}(M_{lmj} + M_{rmj})} \right) \quad (5)$$

The tangential-traction muscle loading model has the highest muscle moment loading efficiency with a value of 83% compared with 65–69% values for the other models. Furthermore, the tangential-traction model required the least amount of applied magnitude of muscle loads to achieve the same bite reaction force. As expected, the loading method that lacked a component of force normal to the skull resulted in an improved ability to generate bite force. Especially for the temporalis muscle group, where normal forces exerted on the skull do not produce significant rotation about the TMJ axis. However, the

tangential-plus-normal-traction model required only approximately 10% more muscle loading force to achieve the same bite reaction force; the two ad hoc models required approximately 25% more muscle loading force. Finally, there is approximately 15% of difference in the magnitudes of the moments exerted about the TMJ axis due to muscle loading in the four models. The ad hoc point-load model resulted in the highest moment about the TMJ axis, and the tangential-plus-normal-traction model resulted in the lowest. Thus, while the muscle moment loading efficiency metric defined in Equation (5) is correlated in some sense with the effectiveness of the applied muscle loads, the unilateral molar bite force is not simply due to a rotational moment exerted about the TMJ axis by the applied muscle forces. Due to the complex geometry of the skull, a more complicated type of mechanical load transfer must be occurring.

### Model Comparison Based on Stress State

The stress states of the four models were compared both qualitatively and quantitatively. For qualitative comparisons, we compared the stress states of the models visually by examining the distribution of the stress tensor field throughout the skull (Figs. 4–7). Except in the vicinity of the point loads in the ad hoc point-load model, all of the models exhibit overall similarity in von Mises stress distributions. However, some differences do exist. For example, the tangential-traction and tangential-plus-normal-traction models produced larger regions of high von Mises stress values within the working-side infratemporal fossa compared with the other two models (Fig. 4). Conversely, the ad hoc point-load model and the ad hoc tangential model resulted in higher stresses along the zygomatic arches (Figs. 4, 5) and the posterior cranial base (Fig. 6). This finding suggests that a greater portion of the applied muscle forces for the two ad hoc models is transmitted to the three constrained nodes (i.e., the bite point and the centers of the TMJs) through the posterior–ventral part of the skull. Such a circuitous force transmission path is inconsistent with an optimal design of a structure with a minimum weight to strength ratio. Indeed, forces transmitted by internal stresses from the dorsal portion of the skull to the posterior-ventral part of the skull have little ability to affect bite force. The constrained nodes defining the center of the TMJs would absorb virtually all of the force offered by this force path by means of increased reaction forces. This is because the constrained nodes at the TMJ are located proximal to the bite point along this circuitous load path, and the very thin nature of this mammalian skull severely limits its ability to transmit loads by transverse shear. With the exception of the ad hoc point load model, there were only minor differences in stress distributions and magnitudes on the dorsal surface of the skull (Fig. 7).

For quantitative comparisons, we selected six identical locations in the four models and compared the results in terms of von Mises stress (Fig. 8). These locations correspond to the centroids of six specific tetrahedral elements that were examined in each model. We chose to report von Mises stress because recent research indicates that cortical bone failure is strain-controlled, which is indicative of ductile fracture (Nalla et al., 2003). The most widely used failure theory for predicting

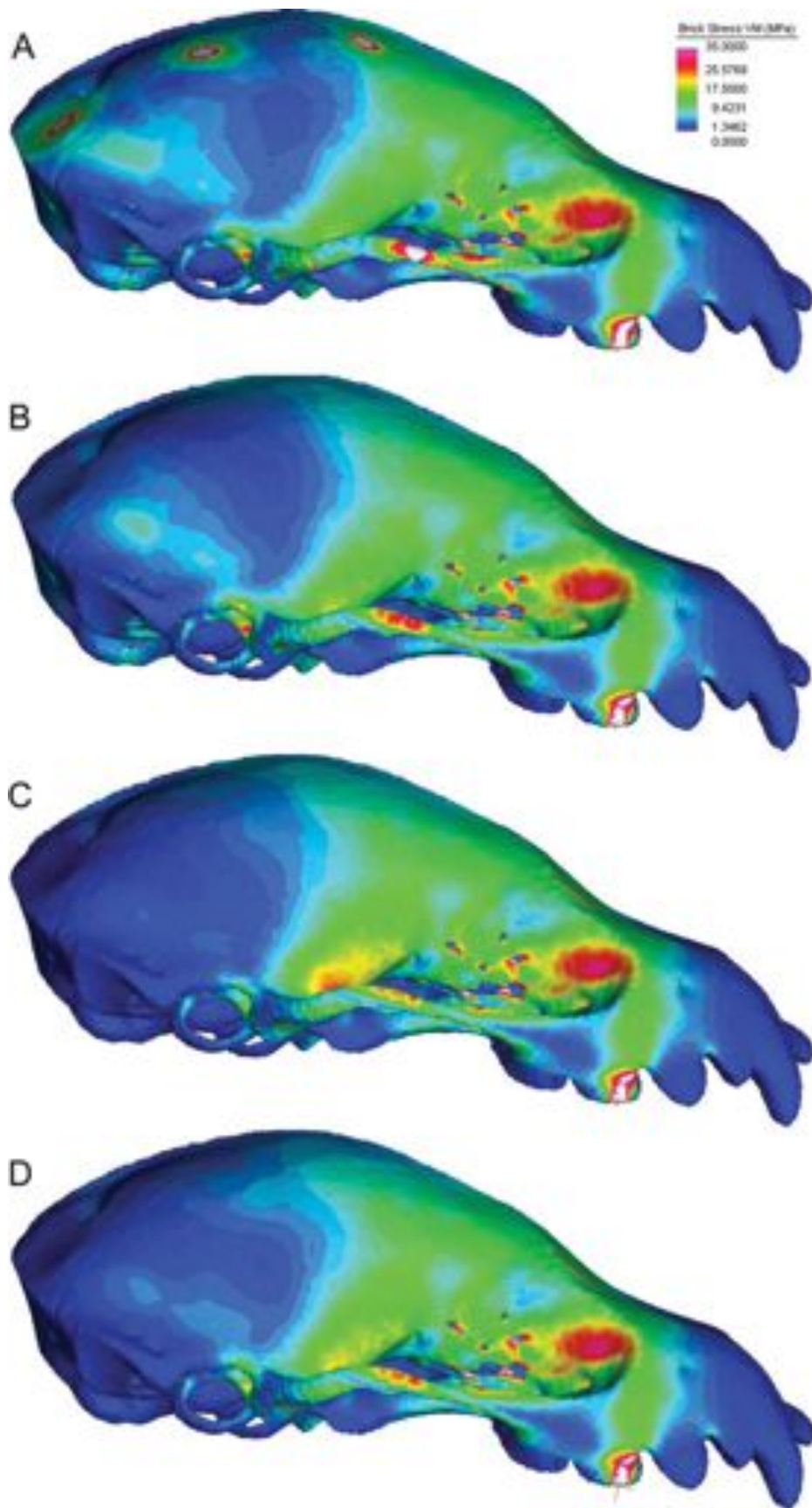


Fig. 4. Left lateral view of the distribution of von Mises stress under the four muscle models. **A–D:** The models are ad hoc point-load (A), ad hoc traction load (B), tangential-traction (C), and tangential-plus-normal-traction (D).

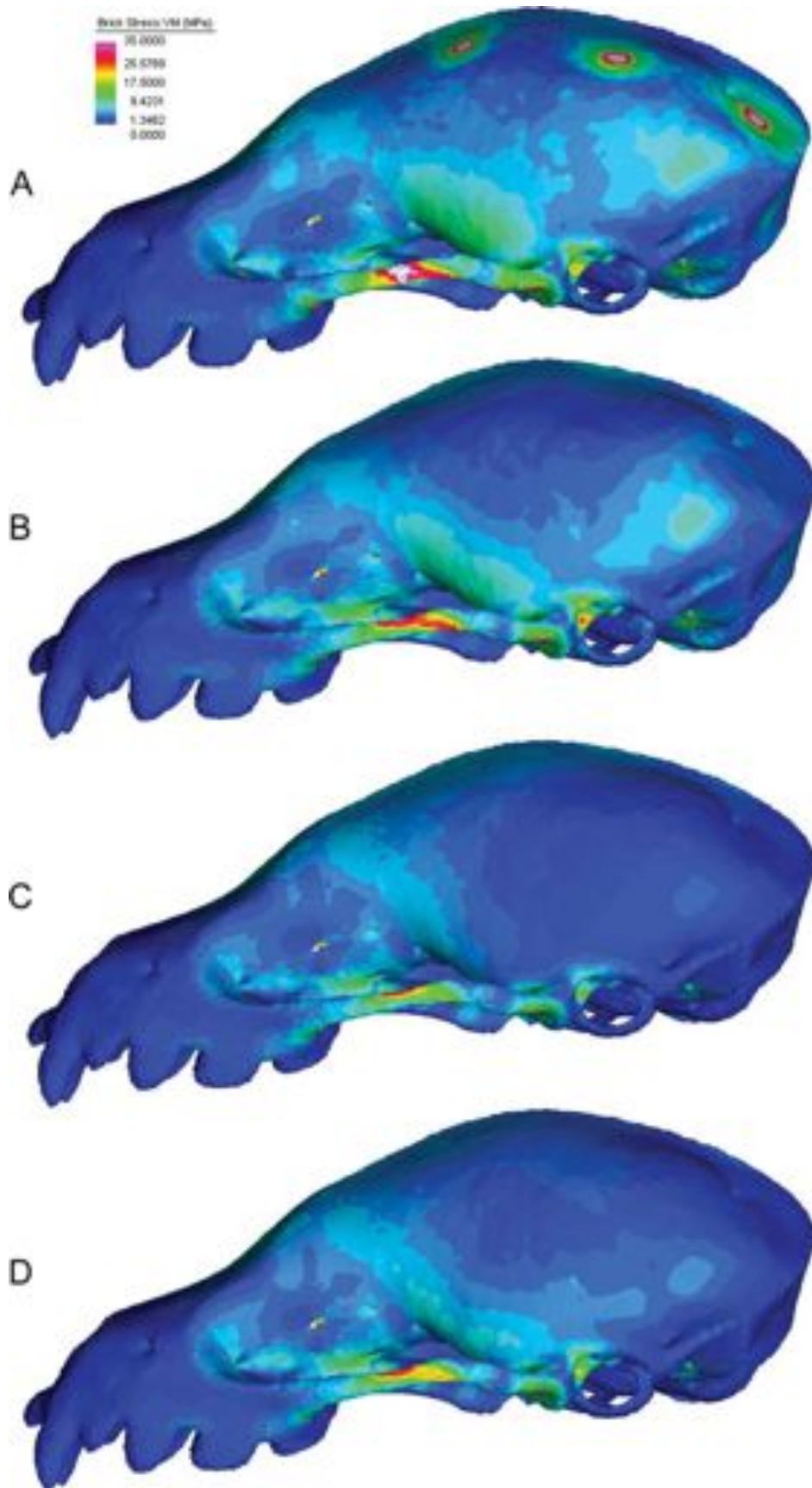


Fig. 5. Right lateral view of the distribution of von Mises stress under the four muscle models. **A–D:** The models are ad hoc point-load (A), ad hoc traction load (B), tangential-traction (C), and tangential-plus-normal-traction (D).

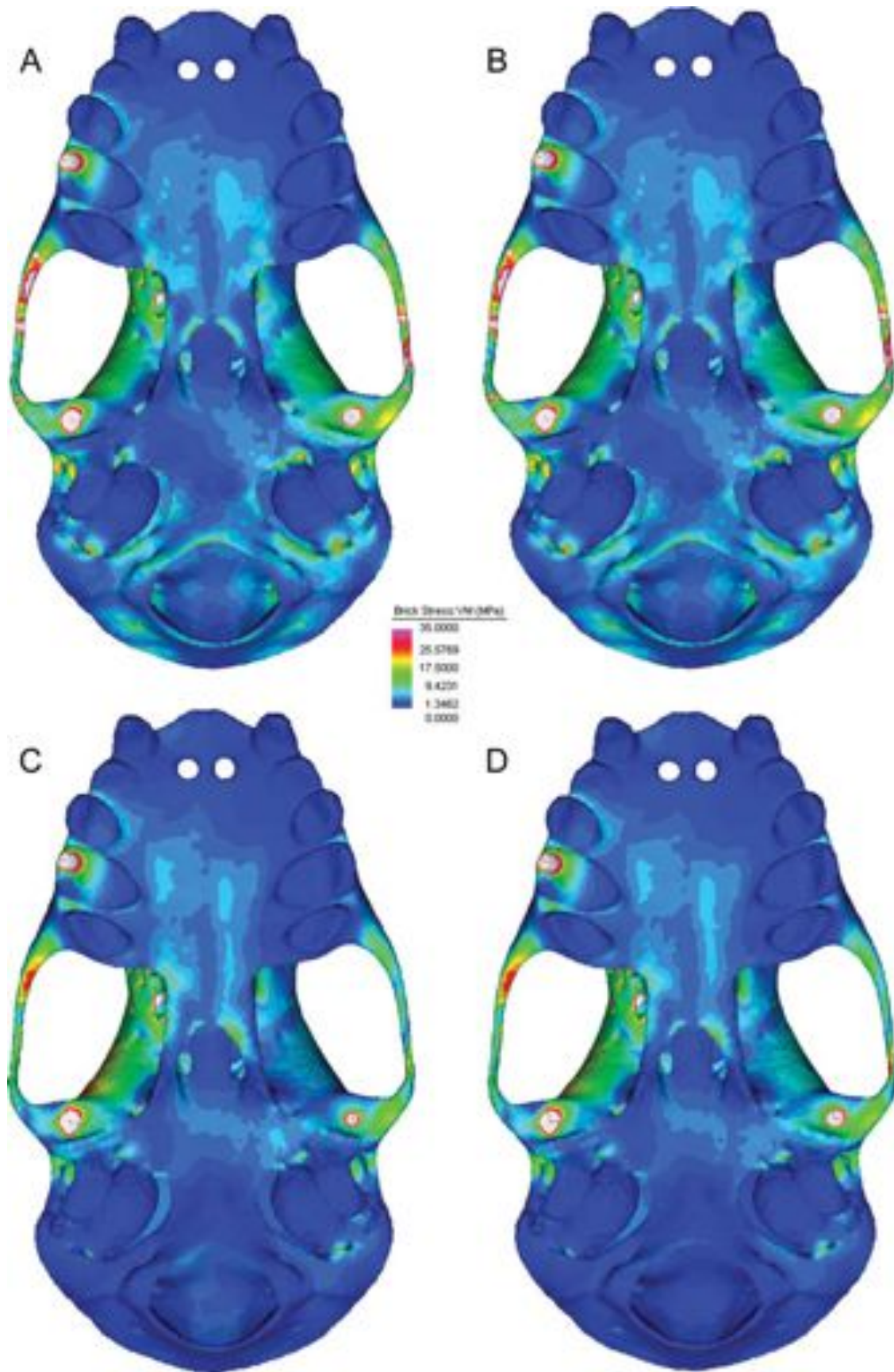


Fig. 6. Dorsal view of the distribution of von Mises stress under the four muscle models. **A–D:** The models are ad hoc point-load (A), ad hoc traction load (B), tangential-traction (C), and tangential-plus-normal-traction (D).

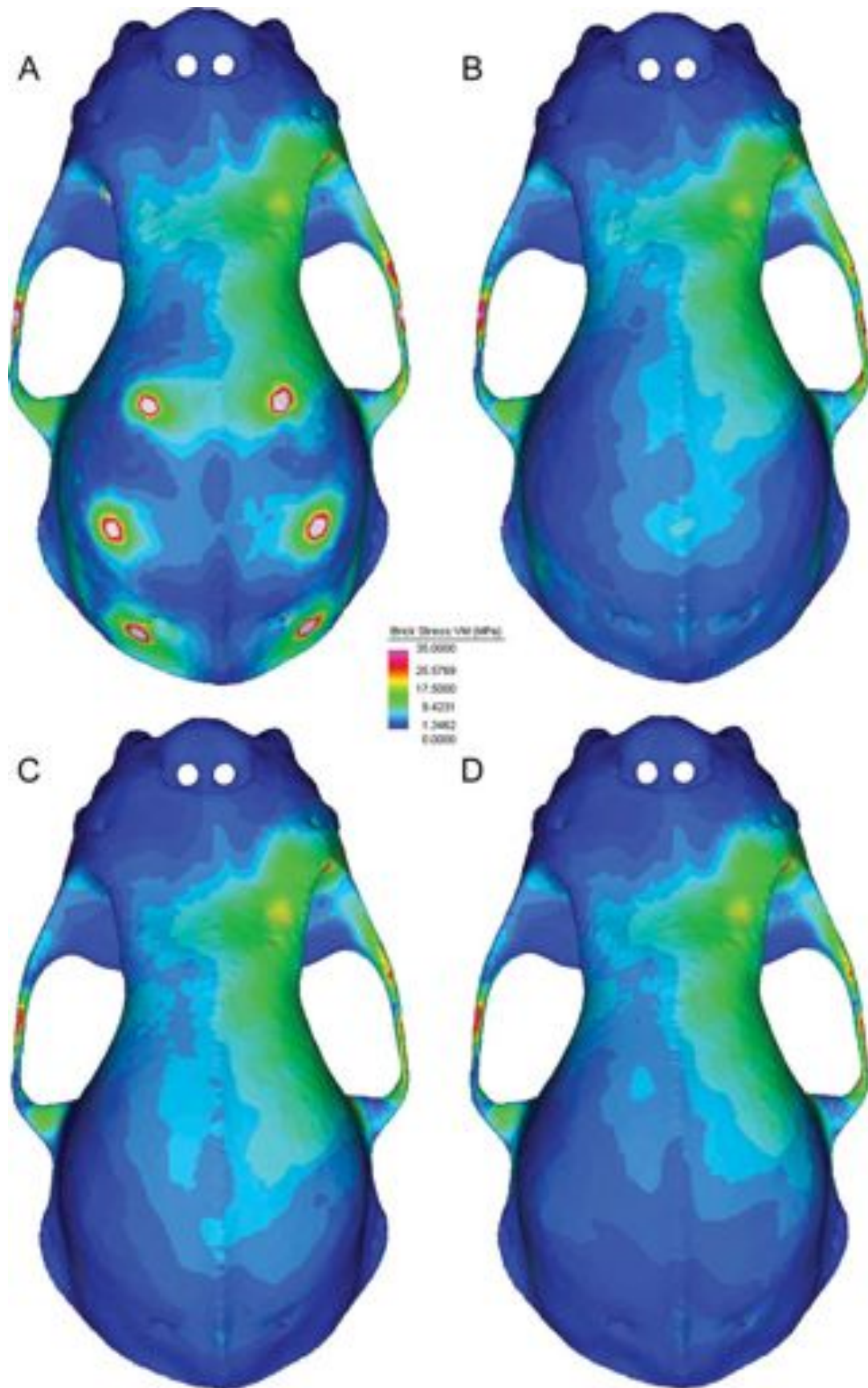


Fig. 7. Ventral view of the distribution of von Mises stress under the four muscle models. **A-D:** The models are ad hoc point-load (A), ad hoc traction load (B), tangential-traction (C), and tangential-plus-normal-traction (D).

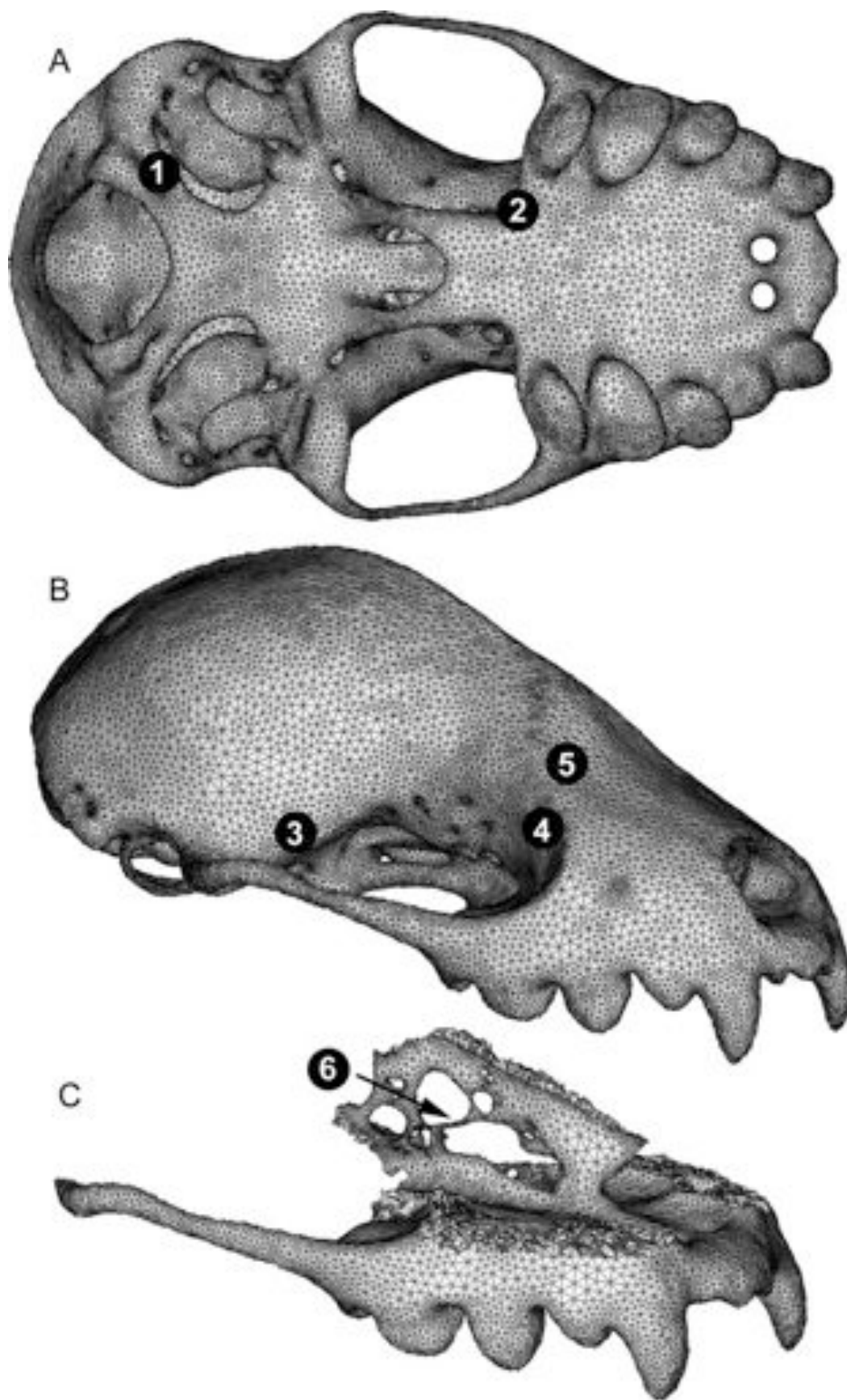


Fig. 8. The six locations selected for quantitative stress item comparisons. Locations are (1) the basioccipital, (2) the palate, (3) the infratemporal fossa, (4) the medial surface of the orbit, (5) the superior surface of the rostrum, and (6) the nasal septum.

**TABLE 2. Comparison of  $\sigma_{11}$ ,  $\sigma_{22}$ ,  $\sigma_{33}$ , and  $\sigma_{vm}$  for the four models at six locations. See Figure 8 for sample locations**

Location	Strain	Stresses for muscle loading models (MPa)			
		<i>ad hoc</i> point load	<i>ad hoc</i> traction	Tangential traction	Tang. + normal traction
Nasal septum	$\sigma_{11}$	13.57	16.97	17.98	17.87
	$\sigma_{22}$	0.33	.041	0.45	0.44
	$\sigma_{33}$	-0.53	-0.70	-0.78	-0.76
	$\sigma_{vm}$	13.69	17.14	18.18	18.06
Palate	$\sigma_{11}$	5.57	9.85	9.75	9.0
	$\sigma_{22}$	0.49	1.07	1.12	1.04
	$\sigma_{33}$	0.27	0.41	0.40	0.42
	$\sigma_{vm}$	5.19	9.13	9.01	8.29
Orbit	$\sigma_{11}$	2.72	3.15	3.25	3.20
	$\sigma_{22}$	0.64	0.51	0.58	0.56
	$\sigma_{33}$	-33.60	-32.95	-33.91	-33.69
	$\sigma_{vm}$	35.32	34.86	35.90	35.65
Rostrum	$\sigma_{11}$	6.36	5.97	6.40	6.35
	$\sigma_{22}$	-0.06	-0.10	-0.03	-0.09
	$\sigma_{33}$	-16.64	-16.75	-17.83	-17.18
	$\sigma_{vm}$	20.56	20.37	21.74	21.06
Infratemporal fossa	$\sigma_{11}$	24.37	25.61	32.68	28.38
	$\sigma_{22}$	5.14	5.46	6.67	6.02
	$\sigma_{33}$	1.42	1.54	1.56	1.32
	$\sigma_{vm}$	21.34	23.26	28.91	25.04
Basioccipital	$\sigma_{11}$	18.43	16.45	2.30	3.55
	$\sigma_{22}$	2.67	2.40	0.34	0.51
	$\sigma_{33}$	2.21	1.97	0.23	0.40
	$\sigma_{vm}$	15.99	14.28	2.02	3.09

ductile failure is the von Mises Failure Criterion, also known as the Maximum Distortional Energy Theorem (Juvinall and Marshek, 1991). Note that the square of the von Mises stress is directly proportional to the distortion strain energy per unit volume. However, we excluded from consideration portions of these regions with artificially high stresses due to modeling idealizations, such as point constraints and point loads. In terms of the principal stresses, von Mises stress is given by

$$\sigma_{vm} = \left[ \frac{1}{2} [(\sigma_{11} - \sigma_{22})^2 + (\sigma_{22} - \sigma_{33})^2 + (\sigma_{11} - \sigma_{33})^2] \right]^{1/2} \quad (6)$$

Apart from a constant, von Mises stress is identical to the octahedral shear stress that exists on a plane equally inclined to three principal stress directions (Cook and Young, 1985). For this reason, von Mises stress is the criterion used to predict failure of ductile materials due to distortion or shear. Note that, because the skull is modeled as a single isotropic homogeneous material, exactly identical comparative results would be obtained by comparing the strain states.

Table 2 presents the principal stresses ( $\sigma_{11}$ ,  $\sigma_{22}$ , and  $\sigma_{33}$ ) and the equivalent or von Mises stress ( $\sigma_{vm}$ ), at these six locations for the four different muscle loading models. Note that because the centroid of a surface tetrahedral element is located interior to the surface, the stress state values shown in Table 2 correspond to interior stress values. However, because the linear tetrahedral element admits only a constant stress state throughout the element volume, these centroidal stress values can be interpreted as occurring on the surface faces of the tetrahedral elements. In the absence of dis-

cretization error, one of the principal stress components must be identically zero on an unloaded or free surface. For each of the six locations for comparison, at least one of the principal stress components is small—but not zero—compared with the other principal stress components. This finding reflects a small amount of discretization error common to all models.

Table 2 reveals many interesting quantitative differences at various locations in the skull. In the nasal septum and palate, there was reasonably good agreement in the stress state for all models except for the point-load model, which under-predicted stresses compared with the other models. The maximum principal stress ( $\sigma_{11}$ ) and von Mises stress ( $\sigma_{vm}$ ) were under-predicted by as much as 40% compared with the tangential-plus-normal model. Qualitative agreement does exist in the sense that all models are predicting essentially a uni-axial tensile stress state at these points, evidenced by the dominant magnitude of the maximum principal stress,  $\sigma_{11}$ , compared with the other two principal stress components,  $\sigma_{22}$  and  $\sigma_{33}$ .

At locations within the inferolateral and superolateral aspects of the rostrum, there was good agreement in all the models for the complete state of stress. Furthermore, apart from stress concentrations due to point loads and point constraints, these rostrum locations exhibited the highest magnitude of von Mises stress in the skull—approximately 35 MPa compared with stress values of 21–28 MPa for the intratemporal fossa location (point E). All models predicted a state of uni-axial compression on the inferolateral aspect of the rostrum, as evidenced by the dominant negative value of  $\sigma_{33}$  compared with the values of  $\sigma_{11}$  and  $\sigma_{22}$ .

Finally, the qualitative observation that the *ad hoc* models yielded much higher stress values on the posterior cranial base than did the mechanics-based models is borne out by the quantitative results (Table 2). Predicted

von Mises stress for the ad hoc models differed from the two mechanics-based loading models by as much as a factor of eight. Indeed, the ad hoc models predicted von Mises stress values on the basioccipital comparable to those predicted in the nasal septum, whereas the tangential model and tangential-plus-normal model predicted stresses five to eight times smaller at the basioccipital compared with the nasal septum.

## DISCUSSION AND CONCLUSIONS

Ideally, these four methods of modeling indirect muscle forces would be validated against in vivo strain gage measurements. Unfortunately, this is not practical for this (and most) bats because their small size imposes significant obstacles to implanting strain gages in most regions of interest (e.g., palate, cranial base, and infratemporal fossa). That said, we believe that a mechanics-based approach to modeling and applying muscle loads will yield a more reliable, repeatable, and accurate loading mechanism than ad hoc muscle modeling methods. Whether or not the reliability and accuracy obtained by the simple-point load modeling methods or the ad hoc traction load modeling models are sufficient depends on the analysis objectives and locations in the skull for which stress values are sought. In the rostrum itself, we found little quantitative difference in terms of the maximum von Mises stress predicted by the various modeling methods, although we did observe that the mechanics-based muscle modeling models predicted larger regions of high von Mises stress compared with the ad hoc models. In other locations, such as the nasal septum, the palate, and the basioccipital, substantial quantitative differences were found in both the size of the stressed region and the maximum stress values.

Certainly, if only a qualitative understanding of the stress and strain distribution in the skull is needed, then either an ad hoc point load or ad hoc traction muscle modeling method provide results that are similar to those derived from mechanics-based muscle loading models, especially in terms of the most highly stressed regions of the skull. For example, the ad hoc models predict a state of uni-axial tension in the nasal septum and palate and a state of uni-axial compression on the superior surface of the rostrum. These states of stress are also predicted by both of the muscle-wrapping mechanics models. Locations of maximum principal stresses and maximum von Mises stresses are virtually the same between all the models once artificial stress concentrations due to point loads and constraints are discounted.

We note that the tangential-traction model and tangential-plus-normal-traction model are in close quantitative agreement with each other in terms of states of stress, except at the infratemporal fossa location where the tangential-traction model predicted a von Mises stress approximately 15% higher than predicted by the tangential-plus-normal-traction. This result occurred despite that approximately 9.4% less total muscle force was applied in the tangential-traction model compared with the tangential-plus-normal-traction model (see Table 1).

One thing is quite clear from our comparative analysis results. Due to the geometric complexity of the skull, it is extremely difficult to know a priori whether or not an ad hoc muscle modeling method will yield sufficiently accurate results in regions of interest. In the case of this

analysis, both the ad hoc point load and ad hoc uniform traction method result in larger percentages of the applied load being transmitted around the posterior region of the skull and then anteriorly through the cranial base to eventually be absorbed by the kinematically constrained TMJ nodes. This force path results in increased reaction forces at the TMJ nodes, a relatively high uni-axial state of tension in the basioccipital region, and an increase in total applied muscle loads to yield the same bite point reaction force compared with the mechanics-based muscle modeling methods.

Ross et al. (2005) used FEA, in vivo data, and principal coordinate analysis to demonstrate that the relative recruitment of masticatory muscles and the latency between muscle activity and maximum bite force can result in substantial variation in maximum shear strain at specific locations on the skull of *Macaca mulatta*. They found that predicted maximum strain varied by a factor of four on the working-side zygomatic arch, while strain at sites in the dorsal interorbital and orbital regions was relatively invariant. Similarly, our results suggest that different masticatory muscle modeling methods can have a substantial quantitative impact on the predicted von Mises stresses at specific locations on the skull. In our modeling experiments, we found relatively low levels of variation except in the basicranium, where the ad hoc point load model predicted between five and eight times more von Mises stress than the two mechanics based models.

By modifying the BoneLoad program to include the capability to read and write finite element data contained in an ASCII (text-based) file structure, the tangential- and tangential-plus-normal-traction modeling approaches could be tested on finite element models developed by other biologists using different commercial FEA programs. This would enable the accuracy of the various modeling approaches presented herein to be assessed on organisms for which in vivo strain data has been or can be obtained. While almost every FEA program has its own unique ASCII file data structure, many tools support, for example, the NASTRAN \*.dat file format. To obtain important validation of our mechanics-based muscle modeling approach, we are currently extending BoneLoad to support this ASCII file structure for FEA model data. This would also enable biologists to quickly and efficiently apply muscle-induced forces consistent with mechanic principles to finite element models in lieu of application of ad hoc muscle forces.

## ACKNOWLEDGMENTS

We thank J.W. Hagadorn for access to the micro-CT scanner and S.F. Werle for constructing the FE model. Technical support provided by Strand7 computing was indispensable in building the BoneLoad program. E.R.D., I.R.G., and J.W.H. were funded by the National Science Foundation (IOS-0447616 and EAR-0236775).

## LITERATURE CITED

- Aguirre LF, Herrel A, van Damme R, Matthyssen E. 2002. Ecomorphological analysis of trophic niche partitioning in a tropical savannah bat community. *Proc Biol Sci* 269:1271–1278.
- Blemker SS, Delp SL. 2005. Three-dimensional representation of complex muscle architectures and geometries. *Ann Biomed Eng* 33:661–673.

- Blemker SS, Pinsky PM, Delp SL. 2005. A 3D model of muscle reveals the causes of nonuniform strains in the biceps brachii. *J Biomech* 38:657–665.
- Cook RD, Young WC. 1985. *Advanced mechanics of materials*. New York: Macmillan Publishing Company.
- De Gueldre G, De Vree F. 1988. Quantitative electromyography of the masticatory muscles of *Pteropus giganteus* (Megachiroptera). *J Morphol* 196:73–106.
- Dumont ER, Herrel A. 2003. The effects of gape angle and bite point on bite force in bats. *J Exp Biol* 206:2117–2123.
- Dumont ER, Piccirillo J, Grosse IR. 2005. Finite-element analysis of biting behavior and bone stress in the facial skeletons of bats. *Anat Rec* 293A:319–330.
- Erickson GM, Cantanese J, Keaveny TM. 2002. Evolution of the biomechanical material properties of the femur. *Anat Rec* 268:115–124.
- Fastnacht M, Hess N, Frey E, Weiser H-P. 2002. Finite element analysis in vertebrate paleontology. *Senckenbergiana lethaea* 82:195–206.
- Hylander WL, Ravosa MJ, Ross C. 2004. Jaw muscle recruitment patterns during mastication in anthropoids and prosimians. In: Anapol F, German RZ, Jablonski NG, editors. *Shaping primate evolution*. Cambridge: Cambridge University Press. p 229–257.
- Johansson T, Meier P, Blickhan R. 2000. A finite-element model for the mechanical analysis of skeletal muscles. *J Theor Biol* 206:131–149.
- Juvinall RC, Marshek KM. 1991. *Fundamentals of machine component design*. New York: John Wiley and Sons.
- Korioth TW, Romilly DP, Hannam AG. 1992. Three-dimensional finite element stress analysis of the dentate human mandible. *Am J Phys Anthropol* 88:69–96.
- Lemos RR, Rokne O, Baranoski GVG, Kawakami Y, Kurihara T. 2005. Modeling and simulating the deformation of human skeletal muscle based on anatomy and physiology. *Comput Animat Virtual Worlds* 16: 319–330.
- Malvern LE. 1969. *Introduction to the mechanics of continuous medium*. Englewood Cliffs, NJ: Prentice-Hall.
- Metzger KA, Daniel WJ, Ross CF. 2005. Comparison of beam theory and finite-element analysis with in vivo bone strain data from the alligator cranium. *Anat Rec A Discov Mol Cell Evol Biol* 283A:331–348.
- Nalla RK, Kinney JH, Ritchie RO. 2003. Mechanistic fracture criteria for the failure of human cortical bone. *Nat Mater* 2:164–168.
- Preuschoft H, Witzel U. 2004. A biomechanical approach to craniofacial shape in primates, using FESA. *Ann Anat* 186:397–404.
- Rayfield EJ. 2004. Cranial mechanics and feeding in *Tyrannosaurus rex*. *Proc Biol Sci* 271:1451–1459.
- Rayfield EJ. 2005. Aspects of comparative cranial mechanics in the theropod dinosaurs *Coelophysis*, *Allosaurus* and *Tyrannosaurus*. *Zool J Linnean Soc* 144:309–316.
- Razdan A, Bae MS. 2005. Curvature estimation scheme for triangle meshes using biquadratic Bézier patches. *Computer-aided Design* 37:1481–1491.
- Richmond BG, Qin Y-X. 1996. Finite element methods in paleoanthropology: the case of phalangeal curvature. *Am J Phys Anthropol Suppl* 22:197.
- Richmond BG, Wright BW, Grosse IR, Dechow PC, Ross CF, Spencer MA, Strait DS. 2005. Finite element analysis in functional morphology. *Anat Rec A Discov Mol Cell Evol Biol* 283A:259–274.
- Ross CF, Patel BA, Slice DE, Strait DS, Dechow PC, Richmond BG, Spencer MA. 2005. Modeling masticatory muscle force in finite element analysis: sensitivity analysis using principal coordinates analysis. *Anat Rec A Discov Mol Cell Evol Biol* 283A:288–299.
- Spears IR, van Noort R, Crompton RH, Cardrew GE, Howard IC. 1993. The effects of enamel anisotropy on the distribution of stress in a tooth. *J Dent Res* 72:1526–1531.
- Strait DS, Richmond B, Ross CF, Spencer M. 2002. Finite-element analysis of a macaque skull: applications for functional morphology. *Am J Phys Anthropol* 34:149.
- Strait DS, Wang Q, Dechow PC, Ross CF, Richmond BG, Spencer MA, Patel BA. 2005. Modeling elastic properties in finite element analysis: how much precision is needed to produce an accurate model? *Anat Rec A Discov Mol Cell Evol Biol* 283A:275–287.
- Teran J, Blemker S, Ng Thow Aing V, Fedkiw R. 2003. Finite volume methods for the simulation of skeletal muscle. *Proceedings of the 2003 ACM/SIGGRAPH/Eurographics Symposium on Computer Animation*, 68–74.
- Teran J, Molino N, Fedkiw R, Bridson R. 2005. Adaptive physics based tetrahedral mesh generation using level sets. *Eng Comput* 21:2–18.
- Ulrich KT, Eppinger SD. 2000. *Product design and development*. 2nd ed. New York: Irwin McGraw Hill.
- Witzel U, Preuschoft H, Sick H. 2004. The role of the zygomatic arch in the statics of the skull and its adaptive shape. *Folia Primatol (Basel)* 75:202–218.
- Wootton RJ, Herbert RC, Young PG, Evans KE. 2003. Approaches to the structural modelling of insect wings. *Philos Trans R Soc Lond B Biol Sci* 358:1577–1587.
- Zhou X, Lu J. 2005. NURBS-based Galerkin method and application to skeletal muscle modeling. *Symposium on Solid and Physical Modeling*, 71–78.

## APPENDIX

### MUSCLE WRAPPING MECHANICS FOR CYLINDRICAL GEOMETRY

In this appendix, we derive formulas for tangential and normal tractions exerted by muscle bundles when they are wrapped around bone structures. Consider a small infinitesimal section of a muscle bundle that is wrapped around a corresponding infinitesimal section of the skull, as shown in Figure 2B. This section spans an infinitesimal angle  $d\theta$  and has a finite radius of curvature  $R(\theta)$ . Note that, although the illustration of Figure 2B indicates that the radius of curvature of the muscle bundle is constant in the wrapped region, in reality it varies considerably in different regions due to variations in the skull's radius of curvature. Our calculations of tangential and normal tractions use vector mathematics to calculate element-by-element variation in radius of curvature in the direction of the muscle fiber.

The free body diagram of the wrapped muscle section (Figure 2B) illustrates that the anchoring of individual muscle fibers over this small section results in a small change in tension in the muscle bundle, i.e., the bundle has more fibers and hence carries more tensile load at the right edge of the muscle section ( $T+dT$ ) than at the left edge ( $T$ ). The anchoring of muscle fibers to the skull results in a tangential traction exerted on the bone. An equal and opposite tangential traction,  $\tau_t$ , is exerted on the muscle fiber as shown. Finally, due the wrapping of this muscle bundle, a normal traction must be exerted by the muscle on the skull, resulting in the equal and opposite normal traction,  $\tau_n$ , exerted on the muscle bundle as shown.

Now, we simply apply Newton's Law of Statics, requiring that this small muscle section remain in static equilibrium, using the normal-tangential coordinate system shown. Recall that the tension  $T$  carried in the muscle bundle has been defined as a force per unit depth. Then, the sum of the forces in the tangential direction yields

$$(T(\theta) + dT)\cos(d\theta/2) - T(\theta)\cos(d\theta/2) - \tau_t R(\theta)d\theta = 0$$

$$dT = \tau_t R(\theta)d\theta \quad (\text{A.1})$$

where the small angle approximation of  $\cos(d\theta/2) \approx 1$  has been used. Integration of Equation (A.1) yields

$$T(\theta) = \int_0^{\theta} dT = \int_0^{\theta} \tau_t R(\theta)d\theta = \tau_t \int_0^{\theta} R(\theta)d\theta = \tau_t s(\theta)$$

$$(\text{A.2})$$

where  $s(\theta)$  is the path length from the far edge of the muscle attachment region to the location defined by the angle  $\theta$ . Now we sum forces in the normal direction for the infinitesimal section of muscle shown in Figure 2B to yield

$$-(T(\theta) + dT) \sin(d\theta/2) - T(\theta) \sin(d\theta/2) + \tau_n R(\theta) d\theta = 0 \implies T(\theta) = \tau_n R(\theta) \quad (\text{A.3})$$

where for small angles the approximation  $\sin(d\theta/2) \approx d\theta/2$  has been used and the term involving  $dT/d\theta$  is neglected as a higher order term. Substituting for  $T(\theta)$  from Equation (A.2) yields

$$\tau_n(\theta) = \left( \frac{s(\theta)}{R(\theta)} \right) \tau_t \quad (\text{A.4})$$

Equation (A.4) was derived using the angle  $\theta$  to define a location on a path in a two-dimensional space. This result can be directly extended to a general surface existing in a three-dimensional space by defining  $\vec{r}$  as a position vector to a point on a surface in a three-dimensional space. Thus, in general,

$$\tau_n(\vec{r}) = \left( \frac{s(\vec{r})}{R(\vec{r})} \right) \tau_t \quad (\text{A.5})$$

where  $s(\vec{r})$  is the path length from the far end of the muscle attachment region to the current location on the surface (i.e., to the centroid of the current element face located by the position vector  $\vec{r}$ ) and  $R(\vec{r})$  is the radius of curvature of the muscle fiber in the direction of the muscle fiber at this location.

A simple example illustrating muscle wrapping mechanics for simplified geometry is presented that validates our derived expressions for normal and tangential tractions due to muscle wrapping. Consider a muscle bundle wrapped 90 degrees around cylinder of radius  $R$  as shown in Figure A1 below. For simplicity, we assume the cylinder and muscle is of unit depth, where depth is the dimension into the plane of the figure. As before, the tension  $T$  of the bundle represents the total muscle bundle force per unit depth. We also assume that the individual fibers are anchored uniformly around the wrapped portion of the cylinder. In a more general case, the muscle fibers are anchored in

wrapped and unwrapped regions of the underlying bone and the fibers may not be anchored uniformly to the skull. At point B ( $x = 0, y = R$ ) in the figure, the muscle bundle carries its full tensile force  $T$ . The vector  $\vec{T}$  at point B is directed to the appropriate muscle insertion point (such as on the lower jaw if this is a skull structure). In reality, these are regions of attachments that are idealized as points that we call force focal nodes. At point A ( $x = R, y = 0$ ), designated as the ‘‘far’’ end of the muscle wrapped region, there is zero amount of tensile force left in the bundle. This cylindrically shaped skull has constant radius of curvature  $R$ , but in general, the curvature of a mammalian skull in the direction of the muscle bundle, as well as other bone structures, varies spatially.

Now consider a small infinitesimal muscle-bundle segment of length  $R(d\vartheta)$  located a circumferential path length  $s(\vartheta)$  from point A as illustrated in the figure. The uniform anchoring of muscle fibers results in a uniform tangential or shear traction  $\tau_t$  exerted on the muscle fiber by the anchoring substrate (i.e., bone) as shown (acting in the  $-\hat{t}$  direction of the local  $\hat{n} - \hat{t}$  coordinate system. In mechanics, a traction load is a force per unit area. The uniform anchoring of muscle fibers requires that

$$\tau_t = \frac{T}{s_{max}} \quad (\text{A.6})$$

where  $s_{max}$  is the path length of wrapped muscle from the far edge of the muscle wrapped region (point A) to the near edge of the muscle wrapped region (point B). Note that for the more general case,  $s_{max}$  would be the path length of the entire wrapped and unwrapped muscle anchoring region. For this simple cylindrical geometry, one has

$$s_{max} = \int_{\vartheta=0}^{\vartheta=\vartheta_{max}} R(\vartheta) d\vartheta = R\vartheta_{max} \text{ where } \vartheta_{max} = \frac{\pi}{2} \quad (\text{A.7})$$

Thus, for this example the tangential traction is given by

$$\tau_t = \frac{T}{R(\pi/2)} = \frac{2T}{\pi R} \quad (\text{A.8})$$

Now we apply Equation (A.4) to compute the normal traction for this simplified geometry:

$$\tau_n(\vartheta) = \left( \frac{s(\vartheta)}{R(\vartheta)} \right) \tau_t = \left( \frac{\int_{\alpha=0}^{\alpha=\vartheta} R(\alpha) d\alpha}{R(\vartheta)} \right) \tau_t \quad (\text{A.9})$$

$$\tau_n(\theta) = \left( \int_{\vartheta=0}^{\vartheta} d\alpha \right) \tau_t = \vartheta \tau_t \quad (\text{A.10})$$

To validate this result, we will compute the total force exerted on the wrapped muscle by the normal and tangential tractions. Theoretically, the total force exerted on the muscle bundle by the skull must be equal and opposite to the pulling force  $T$  acting on the muscle bundle at point B. We resolve components of normal and tangential traction into  $x$  and  $y$  components of forces. This

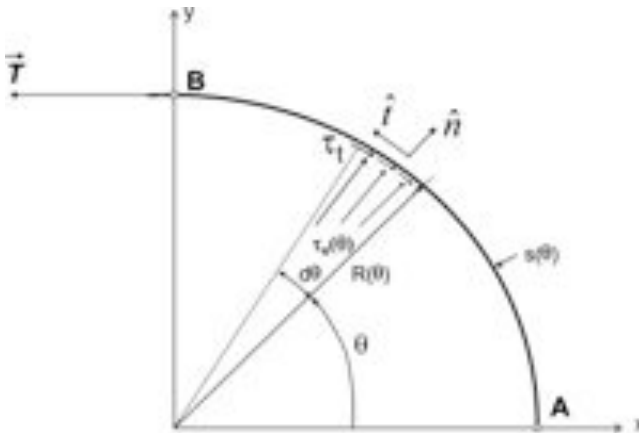


Fig. A1. Example of muscle bundle wrapped and anchored to a cylindrically shaped skull.

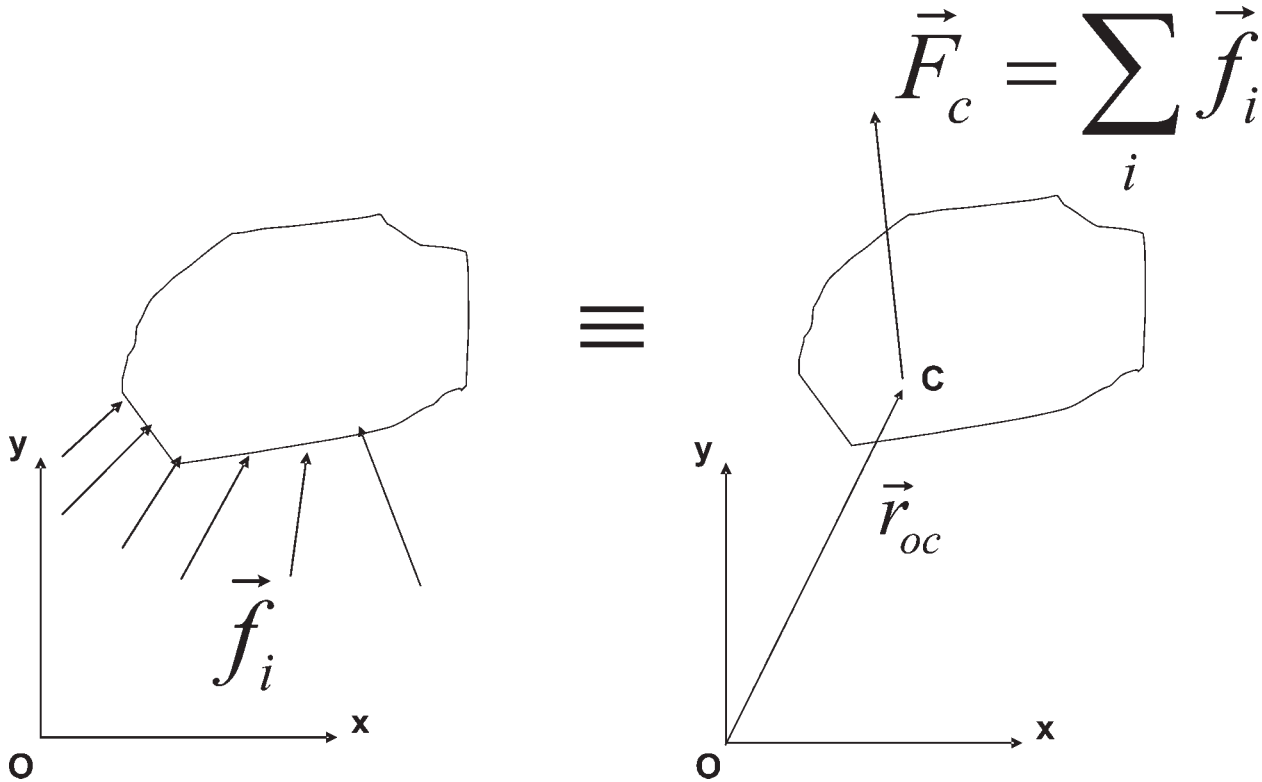


Fig. A2. Force centroid concept.

requires first multiplying the tractions that act over the muscle segment by the area of contact of the infinitesimal muscle section to get force components:

$$\begin{aligned} dF_n &= \tau_n R(\vartheta) d\vartheta = \tau_t R d\vartheta \\ dF_t &= \tau_t R d\vartheta \end{aligned} \tag{A.11}$$

Then, using simple trigonometry, we resolve these components into  $x$  and  $y$  components:

$$\begin{aligned} dF_x &= dF_n \cos(\vartheta) + dF_t \sin(\vartheta) = \tau_t R(\vartheta \cos(\vartheta) + \sin(\vartheta)) d\vartheta \\ dF_y &= dF_n \sin(\vartheta) - dF_t \cos(\vartheta) = \tau_t R(\vartheta \sin(\vartheta) - \cos(\vartheta)) d\vartheta \end{aligned} \tag{A.12}$$

Now we integrate over the wrapped muscle section to get the total  $x$  and  $y$  force components acting on the wrapped muscle bundle due to the constant tangential traction and the varying normal traction:

$$\begin{aligned} F_x &= \int_0^{\theta_{max}} \tau_t R(\vartheta \cos(\vartheta) + \sin(\vartheta)) d\vartheta \\ &= \tau_t R \int_0^{\theta_{max}} (\vartheta \cos(\vartheta) + \sin(\vartheta)) d\vartheta \\ F_y &= \int_0^{\theta_{max}} \tau_t R(\vartheta \sin(\vartheta) - \cos(\vartheta)) d\vartheta \\ &= \tau_t R \int_0^{\theta_{max}} (\vartheta \sin(\vartheta) - \cos(\vartheta)) d\vartheta \end{aligned} \tag{A.13}$$

The integrations can be found in any standard mathematical handbook:

$$\begin{aligned} \int_0^{\theta_{max}} (\vartheta \cos(\vartheta) + \sin(\vartheta)) d\vartheta &= [\theta \sin(\theta)]_0^{\theta_{max}} = \theta_{max} \sin(\theta_{max}) \\ \int_0^{\theta_{max}} (\vartheta \sin(\vartheta) - \cos(\vartheta)) d\vartheta &= [-\theta \cos(\theta)]_0^{\theta_{max}} = -\theta_{max} \cos(\theta_{max}) \end{aligned}$$

Substituting this result into Equation (A.13) yields

$$\begin{aligned} F_x &= \tau_t R \theta_{max} \sin(\theta_{max}) \\ F_y &= -\tau_t R \theta_{max} \cos(\theta_{max}) \end{aligned} \tag{A.14}$$

For this example scenario in which  $\theta_{max} = \pi/2$  we find that

$$\begin{aligned} F_x &= \frac{\tau_t R \pi}{2} \\ F_y &= 0 \end{aligned} \tag{A.15}$$

Substituting for tangential traction  $\tau_t$  using Equation (A.8) yields

$$F_x = \left(\frac{2T}{\pi R}\right) \frac{R\pi}{2} = T \tag{A.16}$$

The result of Equations (A.15) and (A.16) validates, in part, the expressions for the normal and tangential tractions that act on the muscle fiber, as integration results in a total force vector exactly equal and opposite to the tensile force  $T$ , which acts on the muscle bundle in the  $-x$  direction. However, we must still prove that the effec-

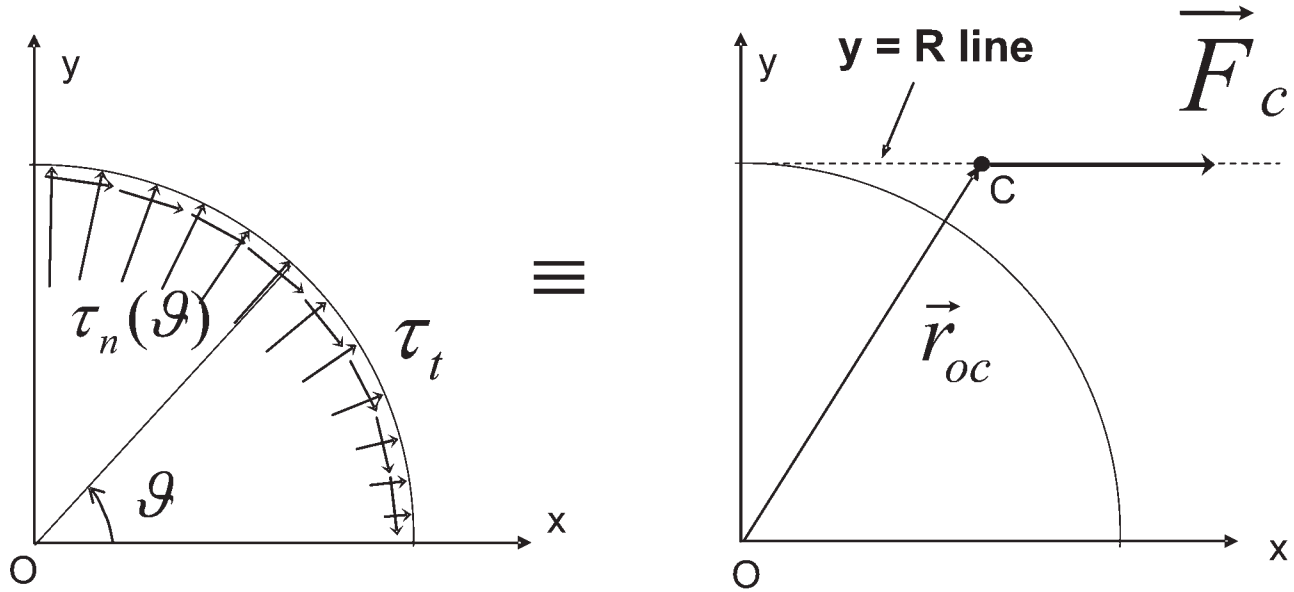


Fig. A3. Equivalent force systems based on system static equilibrium for the wrapped cylinder example problem with normal traction  $\tau_n(\theta)$  given by Equation (A.10) and tangential traction  $\tau_t$  given by Equation (A.6).

tive location of the total force is consistent with static equilibrium principles. This effective location for the total force due to the applied normal and tangential tractions is called the force centroid. The force centroid is the location in which in terms of static equilibrium of the entire system, the set of all applied loads (point loads, tractions, etc.) can be replaced by a single-force vector. This concept is illustrated in Figure A2 below.

The integrations in Equation (A.13) yield the  $x$  and  $y$  components of  $\vec{F}_c$  that are force equivalent from a system static equilibrium perspective to the applied normal and tangentially tractions acting on the muscle bundle. All that remains to be determined is the position vector  $\vec{r}_{oc}$  that locates the point  $c$ , the force centroid, such that “moment” equivalency exists. The moment about a point  $O$  due a force vector acting at another point  $C$  is given by the vector cross product of  $\vec{r}_{oc}$  (the position vector from point  $O$  to point  $C$ ) with the force vector  $\vec{F}_c$ :

$$\vec{M}_O = \vec{r}_{oc} \times \vec{F}_c \tag{A.17}$$

where here the multiplication sign indicates the vector cross product. For static equilibrium equivalency, the moment about any point (moment about a point is a vector that acts at this point; it has units of force-length, such as N mm) due to the set of applied forces and tractions must be identical to the moment about the same point when the set of applied forces and tractions are replaced by the force vector  $\vec{F}_c$  acting at the force centroid. Thus, for the example of Figure A1,

$$\vec{r}_{oc} \times \vec{F}_c = \int_0^{\pi/2} \vec{r}(\theta) \times d\vec{F}(\theta) \tag{A.18}$$

where  $\vec{r}(\theta)$  is the position vector from the coordinate system origin to the small muscle segment and  $d\vec{F}(\theta)$  is

small (i.e. infinitesimal) force vector acting on the small (i.e., infinitesimal) muscle segment due to the applied normal and tangential tractions. Let  $\hat{i}$  and  $\hat{j}$  denote unit vectors acting in the  $x$  and  $y$  direction. The tangential and normal tractions acting on the muscle segment are multiplied by the area of the segment, that is,  $R(\theta)d\theta$ , to yield infinitesimal force components acting in the tangential and normal direction which are then resolved into  $x$  and  $y$  components using basic trigonometry:

$$\begin{aligned} d\vec{F}_t &= \tau_t R(\theta) d\theta (\sin(\theta)\hat{i} - \cos(\theta)\hat{j}) \\ d\vec{F}_n &= \tau_n \theta R(\theta) d\theta (\sin(\theta)\hat{i} + \cos(\theta)\hat{j}) \end{aligned} \tag{A.19}$$

Thus

$$\begin{aligned} d\vec{F} &= d\vec{F}_t + d\vec{F}_n = \tau_t R(\theta) \{(\theta \cos(\theta) + \sin(\theta))\hat{i} \\ &+ (\theta \sin(\theta) - \cos(\theta))\hat{j}\} d\theta \end{aligned} \tag{A.20}$$

The position vector  $\vec{r}(\theta)$  in terms of  $x$  and  $y$  components is

$$\vec{r}(\theta) = R(\theta) (\cos(\theta)\hat{i} + \sin(\theta)\hat{j}) \tag{A.21}$$

For this illustrative problem in which all the forces lie in the  $x$ - $y$  plane, the cross product results in a vector in the out of plane direction (i.e., in the  $z$  direction or unit vector  $\hat{k}$  that acts in the  $z$  direction). Applying Equation (A.18) yields

$$\begin{aligned} (r_{ocx}F_{cy} - r_{ocy}F_{cx})\hat{k} &= \int_0^{\pi/2} [R(\theta) (\cos(\theta)\hat{i} + \sin(\theta)\hat{j}) \\ &\times \tau_t R(\theta) \{(\theta \cos(\theta) + \sin(\theta))\hat{i} + (\theta \sin(\theta) - \cos(\theta))\hat{j}\} d\theta \end{aligned} \tag{A.22}$$

Equation (A.15) gives the components of  $\vec{F}_c$ :  $F_{cx} = \tau_t R(\pi/2)$ ,  $F_{cy} = 0$ . Thus,

$$-r_{ocy}R\tau_t(\pi/2)\hat{k} = R^2\tau_t \int_0^{\pi/2} [\theta \cos(\theta) \sin(\theta) - \cos^2(\theta) - \theta \cos(\theta) \sin(\theta) - \sin^2(\theta)]d\theta \hat{k}$$

Simplifying yields

$$-r_{ocy}R\tau_t(\pi/2)\hat{k} = -R^2\tau_t \int_0^{\pi/2} d\theta \hat{k} = -R^2\tau_t(\pi/2)\hat{k} \quad (\text{A.23})$$

Thus,  $r_{ocy} = R$  and the  $x$  component of  $\vec{r}_{oc}$ ,  $r_{ocx}$ , is indeterminate because  $F_{cy} = 0$ . This means that the force centroid due to the normal and tangential tractions acting on the muscle bundle in this example may be located anywhere horizontally along the line  $y = R$ .  $\vec{F}_c$  is a horizontal force vector acting to the right with a magnitude equal to the muscle tension force  $T$  as shown in Figure A3. Comparing Figures A1 and A2, we note that  $\vec{F}_c + \vec{T} = 0$ , and the sum of the moments due to  $\vec{F}_c$  and  $\vec{T}$  about any point is zero. Thus, our expressions for normal and tangential tractions applied to the muscle bundle by the skull (and conversely equal and opposite tractions applied to the skull by the muscle bundle) yield an effective force vector and a force centroid that satisfy fundamental static equilibrium principles.